

Experimental evidence on the dissipationless transport of chiral edge state of the high-field Chern insulator in MnBi₂Te₄ nanodevices

Zhe Ying^{1,a}, Shuai Zhang^{1,a,*}, Bo Chen^{1,a}, Bin Jia¹, Fucong Fei^{1,*}, Minhao Zhang¹, Haijun Zhang¹, Xuefeng Wang², and Fengqi Song^{1,*}

¹National Laboratory of Solid State Microstructures, Collaborative Innovation Center of Advanced Microstructures, and School of Physics, Nanjing University, Nanjing 210093, China

²National Laboratory of Solid State Microstructures, Collaborative Innovation Center of Advanced Microstructures, and School of Electronic Science and Engineering, Nanjing University, Nanjing 210093, China

^a These authors contributed equally.

*Corresponding authors. Email: S.Z.(szhang@nju.edu.cn), F.F.(feifucong@nju.edu.cn), and F.S.(songfengqi@nju.edu.cn)

Abstract

We demonstrate the dissipationless transport of the chiral edge state (CES) in the nanodevices of quantum anomalous Hall insulator candidate MnBi_2Te_4 . The device presents a near-zero longitudinal resistance together with a quantized Hall plateau in excess of $0.97 h/e^2$ over a range of temperatures from very low up to the Néel temperature of 22 K. Each of four-probe nonlocal measurements gives near-zero resistance and two-probe measurements exhibit a plateau of $+1 h/e^2$, while the results of three-probe nonlocal measurements depend on the magnetic field. This indicates non-dissipation as well as the chirality of the edge state. The CES shows three regimes of temperature dependence, i.e., well-preserved dissipationless transport below 6 K, variable range hopping while increasing the temperature and thermal activation at higher than 22 K. Even at the lowest temperature, a current of over 1.4 μA breaks the dissipationless transport. These form a complete set of evidences of the Chern insulator state in the MnBi_2Te_4 systems.

Introduction

The Hall resistance can be quantized without the formation of the Landau level (LL), which is the case of quantum anomalous Hall effect (QAHE) and also known as the Chern insulator state ¹. Driven by the coexistence of nontrivial topology of the electronic structure and ferromagnetism exchange, the long-desired QAHE was first observed in the magnetically doped topological insulator (TI) Cr-(Bi,Sb)₂Te₃ ². However, inhomogeneity due to the presence of magnetic dopants may lead to a rather small effective magnetic exchange gap, and thus the QAHE onset temperature in a magnetically doped TI is still well below 2 K, despite considerable efforts have been devoted to increasing this ³⁻⁵. MnBi₂Te₄ was predicted and experimentally verified to be an intrinsic magnetic TI ⁶⁻¹⁵, where the magnetism originates from long-range ordered Mn atoms, rather than from stochastically distributed dopants in previous systems. Thus, it becomes a promising platform to allow QAHE and Chern insulator states at higher temperature, as previously observed in recent experiments in flakes of MnBi₂Te₄ ¹⁶⁻²⁰. Even the interesting axion insulator and high Chern number state can be simulated ^{17, 18}. Research enthusiasm is ignited afterwards on the family of MnBi₂Te₄.

Besides the quantized Hall plateaus, dissipationless chiral edge state (CES) should be demonstrated to form a complete set of evidences of Chern insulator states. This is also unique in the future device applications of a Chern insulator device. However, it has been rarely studied and still lack particularly in satisfactory devices with consistent temperature dependence between the CES and Hall plateau.

In this study, we demonstrate the dissipationless transport of the CES in the high-field Chern insulator state of the MnBi_2Te_4 device. The precise quantization of the Chern insulator is observed with a longitudinal resistance of $\sim 0.0002 h/e^2$ and a Hall plateau of $\sim -1.005 h/e^2$, where h is the Planck constant and e is the electron charge. The well-defined quantization can survive up to 22 K, with the plateau being in excess of $0.97 h/e^2$, which allows systematic study of the dissipationless transport of the CES. By considering both the local and nonlocal transport, we studied the temperature-dependent scaling behaviors. The transition from well-preserved dissipationless state to variable range hopping and thermal activation is found with increasing temperature. We also investigate the current-induced breakdown of the dissipationless CES.

Results

Evidences of the high-magnetic-field Chern insulator state.

The MnBi_2Te_4 crystal was grown using the flux method¹³. After mechanical exfoliation and microfabrication, a MnBi_2Te_4 field-effect-transistor was obtained²¹. A hexagonal boron nitride (h-BN) flake was then transferred to the top of the MnBi_2Te_4 to protect the sample, as shown in the inset of **Figure 1a**. During the course of the fabrication, the MnBi_2Te_4 flake was exposed to the atmosphere for a short time only (see Fig. S1 for the details of the fabrications). The MnBi_2Te_4 device discussed in the main text is labeled as Sample 3 (S3). The height of S3 as measured by atomic force microscopy is ~ 7 nm (the inset of **Fig. 1c**), indicating it is a 5 septuple layers (SLs)

device.

The temperature (T) -dependent resistance shows metallic behavior (Fig. 1a). The back-gate-voltage (V_g) -tuned resistance mapping for a range of temperatures from 2 to 40 K is shown in Fig. 1b. Bipolar behavior is shown for V_g varying from -10 V to +60 V, and the charge neutral point (CNP) at low temperature is around +40 V. This implies that the band gap of a MnBi_2Te_4 device is achieved in this range of gate voltages, which provides us with the opportunity to observe the Chern insulator state. The resistance at the CNP (R_{CNP}) is extracted and shown in Fig. 1c. A clear ‘kink’ around 22 K indicates this Néel temperature (T_N) of this sample. It is a little lower than that of the bulk crystal due to the increased thermal fluctuations seen in thinner flakes^{16, 22}. The CNP would be shifted to a higher gate voltage with increasing temperature, especially where the Néel temperature is exceeded. Near the Néel temperature, R_{CNP} is extremely large, at more than 100 k Ω . When $T > 22$ K, R_{CNP} exhibits insulating behavior, which can be described in terms of thermal activation.

The magnetoresistance for different gate voltages is shown in Fig. 1d. When $V_g = +55$ V, the slope of the Hall resistance (R_{xy}) near zero field is negative, while it is positive when $V_g = +33$ V. This implies that the carrier type changes from n - to p -type with decreasing gate voltage from +60 V to -10 V, consistent with the V_g -tuned resistance in Fig. 1b. The high-magnetic-field anomalous Hall effect (AHE) remains negative, independent of the carrier type. Specifically, the quantized anomalous Hall effect (also called the Chern insulator state) is observed when the gate voltage is around the CNP, accompanied by a near-zero longitudinal resistance (R_{xx}) when the magnetic field (B)

is sufficiently strong to polarize the magnetic moment from an antiferromagnetic (AFM) to ferromagnetic (FM) state.

The magnetic field dependent transport is measured in order to characterize the Chern insulator state. The well-defined Chern insulator state is shown in **Figure 2c** when $B = 12$ T and $T = 1.7$ K, with $R_{xx} \sim 0.0002 h/e^2$ and $R_{xy} \sim -1.005 h/e^2$ (see Fig. S4). This indicates the precise quantization of the Chern insulator state. From the V_g dependent resistance at 0 T and 12 T, we find that the CNP is in the quantization regime. This means that the quantization plateau retains its sign in both the n - and p -type regions, which rules out easily the possibility of QHE with LL. R_{xx} and R_{xy} mapping with the magnetic field and gate voltage (Figs. 2a, b) exhibits the quantization regime when $|B| \geq 6$ T. This magnetic field is the transition to the fully polarized FM state.

The temperature-dependent Chern insulator state is also shown. The quantization regime in the resistance mapping at $B = 12$ T (Figs. 2d, e) shrinks clearly with increasing temperature. Below 22 K, the quantization value of $|R_{xy}|$ is larger than $0.97 h/e^2$, and the longitudinal resistance minimum (R_{xx_min}) is less than $0.04 h/e^2$, as shown in Fig. 3a. This is adopted as an indication of the quantization criterion^{3, 4, 16}, and this temperature is the same as the Néel temperature of the sample. The Fermi-level-derived renormalized group (RG) flow²³ in the $(\sigma_{xy}, \sigma_{xx})$ space at 12 T and 2 K is shown in the inset of Fig. 2f. We find that it satisfies the semicircular scaling law (indicated by the dashed red line), which has been studied extensively²⁴. The temperature-dependent converging point extracted from the RG flow is shown in Fig. 2f, which flows to $(-1 e^2/h, 0 e^2/h)$ with decreasing temperature. This implies that

the temperature- and Fermi-level-dependence of the RG flow provide a good description of the Chern insulator state.

Validation of the dissipationless transport of the CES.

The systematic temperature dependence of the dissipationless CES is studied. In **Figure 3a**, the temperature-dependent longitudinal resistance minimum and quantized anomalous Hall resistance in the quantization regime is shown. We note that the temperature can be divided into three regimes. When $T \leq 6$ K (regime I), R_{xx_min} is around 14 Ω , and it remains almost unchanged as indicated by the pink box in Fig. 3b. Such a small value of R_{xx_min} is a hallmark of the well-preserved dissipationless CES of a Chern insulator. When $T > 6$ K, R_{xx_min} increases sharply, which implies the breakdown of the dissipationless CES. When $6 \text{ K} < T < 22 \text{ K}$ (regime II), R_{xx_min} changes from 36 to 1006 Ω . The linear relationship between $\ln T \cdot R_{xx_min}$ and $T^{-1/2}$ in this temperature regime (the dashed red line in Fig. 3c) indicates that the transport behavior can be described by variable range hopping (VRH)²⁵⁻²⁷. The temperature-induced breakdown may thus be attributed to VRH. When $T > 22$ K (regime III), an Arrhenius plot with $R_{xx_min} \propto \exp(-T_0/T)$ reveals the thermal activation behavior (Fig. 3d), where $T_0 = \Delta E/2k_B$, ΔE is the thermal activation gap, and k_B is the Boltzmann constant. The gap extracted from the fit is $T_0 \sim 92$ K. Additionally, the transition temperature from VRH to thermal activation is also about the same as the Néel temperature of 22 K.

At the same time, the R_{sh} - B curves in regime I reveal a critical magnetic field (B_C).

The four curves intersect at a point near critical magnetic field of -4.36 T (the inset of Fig. 3e). In the vicinity of B_C , we can plot the scaling behavior^{17, 28-31} of $\ln R_{sh} \sim \ln(|B - B_C|/T^\kappa)$, as shown in Fig. 3e. Here, these curves would merge into one single curve, with the critical resistance being about $1.2 h/e^2$ and the exponent parameter $\kappa \sim 0.35$. The two parameters are similar to those seen in other systems, such as the transition from QAH state to Anderson insulator²⁸, the transition from axion insulator to Chern insulator¹⁷, the quantum Hall plateau transition²⁹, and so on. This finding implies that the transition here also shares the same universality class³².

The current (I)-dependent transport has also attracted significant interest³³, especially the current-induced breakdown of the quantization³⁴. At 2 K, the values of longitudinal resistance minimum in the quantization regime for different currents are shown in Fig. 3f. We find that R_{xx_min} stays around 14 Ω when the current is less than 1.4 μA , and starts to increase more obviously when $I > 1.4 \mu\text{A}$. Thus, the critical current (I_C) for the breakdown of the quantization can be identified as 1.4 μA at 2 K. The critical currents at different temperatures are shown in Fig. 3g, and the value decreases with increasing temperature. Furthermore, I_C exhibits an almost linear relationship with temperature. Therefore, the effect of current on quantization may be similar to that of temperature. The current-induced breakdown of the dissipationless CES can be account for by two mechanisms, i.e., electric-field-driven VRH³⁵ and bootstrap electron heating^{36, 37}. The breakdown that originates from bootstrap electron heating in QHE is often characterized by a large critical current (tens of μA)^{38, 39}, and there is usually an abrupt increase in the resistance^{39, 40}. However, in this

case the critical current for the Chern insulator state is relatively small (near 1 μA) here, and an abrupt jump is not seen. Therefore, the current-induced breakdown cannot be explained by electron heating in this case. In our work, the current-induced breakdown resistance is a few tens of Ohms (Fig. 3f), and it is as small as the resistance minimum in the VRH region. The small breakdown resistance, together with the linear relationship between the critical current and the temperature, suggests that the electric-field-driven VRH is the origin of the breakdown. The area shaded yellow in Fig. 3g thus marks the well-preserved dissipationless CES, and the part to the right of the dashed red line is the VRH region.

Nonlocal measurement demonstrating the dissipationless CES.

Nonlocal measurement with different probes is used to verify the dissipationless CES. The two-probe resistance $R_{12/12}$ ($= V_{12}/I_{12}$), three-probe resistance $R_{16/12}$ ($= V_{16}/I_{12}$), and four-probe resistance $R_{65/12}$ ($= V_{65}/I_{12}$) are shown against B in **Figure 4a**. The inset indicates the numbers of the measurement probes. The two-probe resistance $R_{12/12}$ always exhibits a plateau of $+1 h/e^2$ at both positive and negative magnetic field when it settles into the quantization regime (here $V_g = 45$ V and $T = 1.7$ K), and the four-probe resistance $R_{65/12}$ is always near $0 h/e^2$. It is the direct feature of the CES of a Chern insulator. Differently, the three-probe resistance $R_{16/12}$ is $+1 h/e^2$ in the negative magnetic field, and $0 h/e^2$ in the positive field, which can be explained easily by the Landauer-Büttiker formalism^{41, 42}. In a positive magnetic field, clockwise channel chirality is expected, and the voltage potentials are $V_1 = V_6 = V_5 = V_4 = V_3$,

thus V_{16} should be equal to V_{65} , which is zero. Therefore, $R_{16/12} = R_{65/12} = 0 h/e^2$. In a negative magnetic field, however, the voltage potentials are $V_6 = V_5 = V_4 = V_3 = V_2$, thus V_{16} should be equal to V_{12} , showing $R_{16/12} = R_{12/12} = +1 h/e^2$. The chirality of the edge state is thus shown convincingly.

The temperature-dependent four-probe nonlocal resistance $R_{23/16}$ is shown in Fig. 4b. Like the longitudinal resistance in Fig. 2e, $R_{23/16}$ exhibits similar behavior. Values in the quantization regime ($R_{23/16_min}$) at 12 T are extracted in order to confirm the dissipationless transport, and there are also three temperature regimes. In Fig. 4c, when the temperature is no more than 6 K, $R_{23/16_min}$ is less than 5 Ω , suggesting well-preserved dissipationless CES. This can be explained by VRH between 6 K and 22 K, and by thermal activation over 22 K (in Figs. 4d, e). The thermal activation gap of the nonlocal measurement from the Arrhenius fitting is $T_{nl} \sim 85$ K, while the nonlocal thermal activation gap is consistent with the local thermal activation gap $T_0 \sim 92$ K. In Fig. 4f, the plateau width ΔV_g , defined as the difference between the peak and the valley in dR/dV_g (the yellow circles in Fig. 4b), is extracted. At 2 K, the width can be as large as 15 V. It decreases with increasing temperature, and the nonlocal and local measurements exhibit the similar width. Consequently, nonlocal measurements reveal the dissipationless CES of the Chern insulator well, which has been widely studied in QHE and quantum spin Hall effect⁴³. Both local and nonlocal measurements are effective methods for detecting the characteristics of the edge state.

Conclusions

In summary, we have observed the precise quantization of the Chern insulator state in the MnBi_2Te_4 device, with the well-defined quantization being maintained up to the Néel temperature of 22 K. Nonlocal measurements confirm the dissipationless CES of the Chern insulator. The transport behavior of the dissipationless CES was studied systematically by both local and nonlocal measurement. An increase in temperature increasing leads to three different regimes, i.e., well-preserved dissipationless CES, VRH and thermal activation. The increasing of the current can induce the breakdown of the well-preserved dissipationless CES, which is attributed to the electric-field-driven VRH. Our work reveals the novel scaling physics, and forms a complete set of evidences on the Chern insulator state in MnBi_2Te_4 .

Methods

Crystal Growth. The MnBi_2Te_4 crystal was grown by the flux method. MnTe and Bi_2Te_3 were mixed in an alumina crucible with a molar ratio of 1:5.85, and then sealed in a quartz ampule. The mixture was heated to $950\text{ }^\circ\text{C}$ over a period of one day. After maintaining it at a temperature of $950\text{ }^\circ\text{C}$ for 12 h, it was cooled slowly to $580\text{ }^\circ\text{C}$. The MnBi_2Te_4 crystals were then obtained by centrifugation.

Device Fabrication. Thin flakes of MnBi_2Te_4 were exfoliated by tape, and then stamped on the 300-nm SiO_2 coated Si substrate. A few layers of graphite were transferred on to the MnBi_2Te_4 flake to protect the sample from the air and the photoresist. The graphite was transferred away prior to the electron beam lithography, and the gold electrode was then deposited. Following the lift-off process, the MnBi_2Te_4 field-effect-transistor was obtained. Finally, the h-BN was transferred on to the top of the MnBi_2Te_4 for protection. The transfer process was carried out in a glove box with the O_2 and H_2O each less than 0.1 ppm. Over the whole course of the fabrication, the MnBi_2Te_4 was exposed to air for a very short time (also see Fig. S1).

Transport Measurement. Electrical transport measurements were performed at temperatures down to 1.7 K and magnetic field up to 12 T. The voltage difference between different probes was measured using standard lock-in amplifiers (Stanford Research 830) with low frequency (13 Hz), and the back gate was applied using Keithley 2400 source meter. Except for the current-dependent transport shown in Figs. 3f, g, the current applied between the source and the drain was 100 nA. The longitudinal and Hall resistances are defined as $R_{xx} = V_{23}/I_{14}$ and $R_{xy} = V_{26}/I_{14}$, while the probe numbers are illustrated in the inset of Fig. 4a. The nonlocal resistance is defined in the main text, and the sheet resistance is given by $R_{sh} = R_{xx}(W/L)$, where L and W are the channel length and width, respectively. The conductivity is given by $\sigma_{xx} = R_{sh}/(R_{sh}^2 + R_{xy}^2)$ and $\sigma_{xy} = R_{xy}/(R_{sh}^2 + R_{xy}^2)$. The RG flow is plotted with σ_{xy} on the abscissa and σ_{xx} on the ordinate in $(\sigma_{xy}, \sigma_{xx})$ space.

Acknowledgments

We gratefully acknowledge the financial support of the National Key R&D Program of China (No. 2017YFA0303203), the National Natural Science Foundation of China (Grant Nos. U1732273, U1732159, 12025404, 12074181, 11904165, 11904166, 61822403, 11874203, 11834006, 91622115, 11522432, and 11574217), the Natural Science Foundation of Jiangsu Province (Grant Nos. BK20200007, BK20190286, BK20200312, and BK20200310), the Fundamental Research Funds for the Central Universities (Nos. 021314380147, 020414380149, 020414380150, 020414380151, and 020414380152), the Users with Excellence Project of Hefei Science Center CAS (No. 2019HSC-UE007), and the opening Project of the Wuhan National High Magnetic Field Center.

Author contributions

Z.Y. fabricated the devices. Z.Y. and S.Z. performed the transport measurements. B.C. and F.F. grew the bulk crystals. S.Z., Z.Y. and F.S. wrote the manuscript with comments from all authors. F.S. was responsible for overall project planning and direction.

Data Availability

The data in this work are available from the corresponding author upon reasonable request.

Reference

1. Haldane, F. D. M. Model for a Quantum Hall Effect without Landau Levels: Condensed-Matter Realization of the "Parity Anomaly". *Physical Review Letters* **61**, 2015-2018 (1988).
2. Chang, C.-Z. *et al.* Experimental Observation of the Quantum Anomalous Hall Effect in a Magnetic Topological Insulator. *Science* **340**, 167-170 (2013).
3. Mogi, M. *et al.* Magnetic modulation doping in topological insulators toward higher-temperature quantum anomalous Hall effect. *Applied Physics Letters* **107**, 182401 (2015).
4. Ou, Y. *et al.* Enhancing the Quantum Anomalous Hall Effect by Magnetic Codoping in a Topological Insulator. *Advanced Materials* **30**, 1703062 (2018).
5. Pan, L. *et al.* Probing the low-temperature limit of the quantum anomalous Hall effect. *Science Advances* **6**, eaaz3595 (2020).
6. Gong, Y. *et al.* Experimental Realization of an Intrinsic Magnetic Topological Insulator. *Chinese Physics Letters* **36**, 076801 (2019).
7. Otrokov, M. M. *et al.* Prediction and observation of an antiferromagnetic topological insulator. *Nature* **576**, 416-422 (2019).
8. Zhang, D. *et al.* Topological Axion States in the Magnetic Insulator MnBi_2Te_4 with the Quantized Magnetoelectric Effect. *Physical Review Letters* **122**, 206401 (2019).
9. Li, J. *et al.* Intrinsic magnetic topological insulators in van der Waals layered MnBi_2Te_4 -family materials. *Science Advances* **5**, eaaw5685 (2019).
10. Yan, J. Q. *et al.* Crystal growth and magnetic structure of MnBi_2Te_4 . *Physical Review Materials* **3**, 064202 (2019).
11. Zeugner, A. *et al.* Chemical Aspects of the Candidate Antiferromagnetic Topological Insulator MnBi_2Te_4 . *Chemistry of Materials* **31**, 2795-2806 (2019).
12. Otrokov, M. M. *et al.* Unique Thickness-Dependent Properties of the van der Waals Interlayer Antiferromagnet MnBi_2Te_4 Films. *Physical Review Letters* **122**, 107202 (2019).
13. Chen, B. *et al.* Intrinsic magnetic topological insulator phases in the Sb doped MnBi_2Te_4 bulks and thin flakes. *Nature Communications* **10**, 4469 (2019).
14. Pei, C. *et al.* Pressure-Induced Topological and Structural Phase Transitions in an Antiferromagnetic Topological Insulator. *Chin. Phys. Lett.* **37**, 066401 (2020).
15. Zhang, J. *et al.* Large Dynamical Axion Field in Topological Antiferromagnetic Insulator $\text{Mn}_2\text{Bi}_2\text{Te}_5$. *Chin. Phys. Lett.* **37**, 077304 (2020).
16. Deng, Y. *et al.* Quantum anomalous Hall effect in intrinsic magnetic topological insulator MnBi_2Te_4 . *Science* **367**, 895-900 (2020).
17. Liu, C. *et al.* Robust axion insulator and Chern insulator phases in a two-dimensional antiferromagnetic topological insulator. *Nature Materials* **19**, 522-527 (2020).
18. Ge, J. *et al.* High-Chern-number and high-temperature quantum Hall effect without Landau levels. *National Science Review* **7**, 1280-1287 (2020).
19. Liu, C. *et al.* Helical Chern insulator phase with broken time-reversal symmetry in MnBi_2Te_4 . *arXiv:2001.08401* (2020).
20. Ovchinnikov, D. *et al.* Intertwined Topological and Magnetic Orders in Atomically Thin Chern Insulator MnBi_2Te_4 . *arXiv:2011.00555* (2020).
21. Zhang, S. *et al.* Experimental Observation of the Gate-Controlled Reversal of the

- Anomalous Hall Effect in the Intrinsic Magnetic Topological Insulator MnBi₂Te₄ Device. *Nano Letters* **20**, 709-714 (2020).
22. Yang, S. *et al.* Odd-Even Layer-Number Effect and Layer-Dependent Magnetic Phase Diagrams in MnBi₂Te₄. *Phys. Rev. X* **11**, 011003 (2021).
 23. Khmelnitskii, D. E. Quantization of Hall conductivity. *JETP Lett* **38**, 552-556 (1983).
 24. Checkelsky, J. G. *et al.* Trajectory of the anomalous Hall effect towards the quantized state in a ferromagnetic topological insulator. *Nature Physics* **10**, 731-736 (2014).
 25. Polyakov, D. G. & Shklovskii, B. I. Variable range hopping as the mechanism of the conductivity peak broadening in the quantum Hall regime. *Physical Review Letters* **70**, 3796-3799 (1993).
 26. Hohls, F., Zeitler, U. & Haug, R. J. Hopping Conductivity in the Quantum Hall Effect: Revival of Universal Scaling. *Physical Review Letters* **88**, 036802 (2002).
 27. Xie, F. *et al.* Phase transition and anomalous scaling in the quantum Hall transport of topological-insulator Sn-Bi_{1.1}Sb_{0.9}Te₂S devices. *Physical Review B* **99**, 081113 (2019).
 28. Chang, C.-Z. *et al.* Observation of the Quantum Anomalous Hall Insulator to Anderson Insulator Quantum Phase Transition and its Scaling Behavior. *Physical Review Letters* **117**, 126802 (2016).
 29. Shahar, D., Tsui, D. C., Shayegan, M., Bhatt, R. N. & Cunningham, J. E. Universal Conductivity at the Quantum Hall Liquid to Insulator Transition. *Physical Review Letters* **74**, 4511-4514 (1995).
 30. Wu, X. *et al.* Scaling behavior of the quantum phase transition from a quantum-anomalous-Hall insulator to an axion insulator. *Nature Communications* **11**, 4532 (2020).
 31. Liu, C. *et al.* Distinct Quantum Anomalous Hall Ground States Induced by Magnetic Disorders. *Phys. Rev. X* **10**, 041063 (2020).
 32. Kivelson, S., Lee, D.-H. & Zhang, S.-C. Global phase diagram in the quantum Hall effect. *Physical Review B* **46**, 2223-2238 (1992).
 33. Polyakov, D. G. & Shklovskii, B. I. Conductivity-peak broadening in the quantum Hall regime. *Physical Review B* **48**, 11167-11175 (1993).
 34. Nachtwei, G. Breakdown of the quantum Hall effect. *Physica E: Low-dimensional Systems and Nanostructures* **4**, 79-101 (1999).
 35. Kawamura, M. *et al.* Current-Driven Instability of the Quantum Anomalous Hall Effect in Ferromagnetic Topological Insulators. *Physical Review Letters* **119**, 016803 (2017).
 36. Komiyama, S. & Kawaguchi, Y. Heat instability of quantum Hall conductors. *Physical Review B* **61**, 2014-2027 (2000).
 37. Fox, E. J. *et al.* Part-per-million quantization and current-induced breakdown of the quantum anomalous Hall effect. *Physical Review B* **98**, 075145 (2018).
 38. Okuno, T. *et al.* Electron Concentration and Mobility Dependence of Breakdown of the Quantum Hall Effect. *Journal of the Physical Society of Japan* **64**, 1881-1884 (1995).
 39. Eber, G., Klitzing, K. v., Ploog, K. & Weinmann, G. Two-dimensional magneto-quantum transport on GaAs-Al_xGa_{1-x}As heterostructures under non-ohmic conditions. *Journal of Physics C: Solid State Physics* **16**, 5441-5448 (1983).
 40. Cage, M. E. *et al.* Dissipation and Dynamic Nonlinear Behavior in the Quantum Hall Regime. *Physical Review Letters* **51**, 1374-1377 (1983).

41. Bestwick, A. J. *et al.* Precise Quantization of the Anomalous Hall Effect near Zero Magnetic Field. *Physical Review Letters* **114**, 187201 (2015).
42. Büttiker, M. Absence of backscattering in the quantum Hall effect in multiprobe conductors. *Physical Review B* **38**, 9375-9389 (1988).
43. Roth, A. *et al.* Nonlocal Transport in the Quantum Spin Hall State. *Science* **325**, 294-297 (2009).

Figure Captions

Figure 1. Observation of the Chern insulator state in MnBi_2Te_4 .

a Temperature dependent resistance. The inset shows the optical graph of the device, and the white scale bar is $20\ \mu\text{m}$. **b** Gate voltage-dependent resistance mapping at various temperatures, showing the bipolar behavior with gate voltage. **c** The resistance of the charge neutral point (R_{CNP}) extracted from **a** exhibits the ‘kink’ around 22 K, which is the Néel temperature of the sample. The inset is the atomic force microscopy graph, and shows that the height of the sample is $\sim 7\ \text{nm}$. The white scale bar is $1\ \mu\text{m}$. **d** The magneto-transport for various gate voltages when $T = 1.7\ \text{K}$. Near the charge neutral point, the quantized anomalous Hall effect is observed.

Figure 2. Magnetic and temperature dependent chiral edge state.

a R_{xy} mapping with gate voltage and magnetic field at 1.7 K. **b** R_{xx} mapping with gate voltage and magnetic field at 1.7 K. **c** Gate-dependent R_{xy} and R_{xx} at 1.7 K and 12 T. **d** R_{xy} mapping with gate voltage and temperature at 12 T. **e** R_{xx} mapping with gate voltage and temperature at 12 T. **f** Temperature-dependent converging points extracted from RG flow at 12 T. The inset shows the RG flow at 1.7 K and 12 T.

Figure 3. Scaling of the dissipationless chiral edge state.

a Temperature-dependent longitudinal resistance minimum ($R_{\text{xx_min}}$) and quantized Hall resistance. **b** Well-preserved dissipationless CES below 6 K, with $R_{\text{xx_min}}$ around $14\ \Omega$. **c** VRH fitting. **d** Thermal activation fitting. **e** Scaling analysis in the vicinity of the critical magnetic field with the relationship $\ln R_{\text{sh}} \sim \ln(|B - B_{\text{C}}|/T^{\kappa})$. The inset shows the critical magnetic field $\sim 4.36\ \text{T}$. **f** Current-induced breakdown of the dissipationless CES at 2 K, with the critical current being $\sim 1.4\ \mu\text{A}$. **g** Temperature-dependent critical current.

Figure 4. Nonlocal measurement of the dissipationless chiral edge state.

a Two-probe resistance $R_{12/12}$, three-probe resistance $R_{16/12}$, and four-probe resistance $R_{65/12}$ at 45 V and 1.7 K, from top to bottom. The inset defines the measurement

probes numbers. **b** Nonlocal four-probe resistance $R_{23/16}$ mapping with gate voltage and temperature at 12 T. **c** Well-preserved dissipationless CES below 6 K. **d** VRH fitting. **e** Thermal activation fitting. **f** Plateau width at different temperatures.

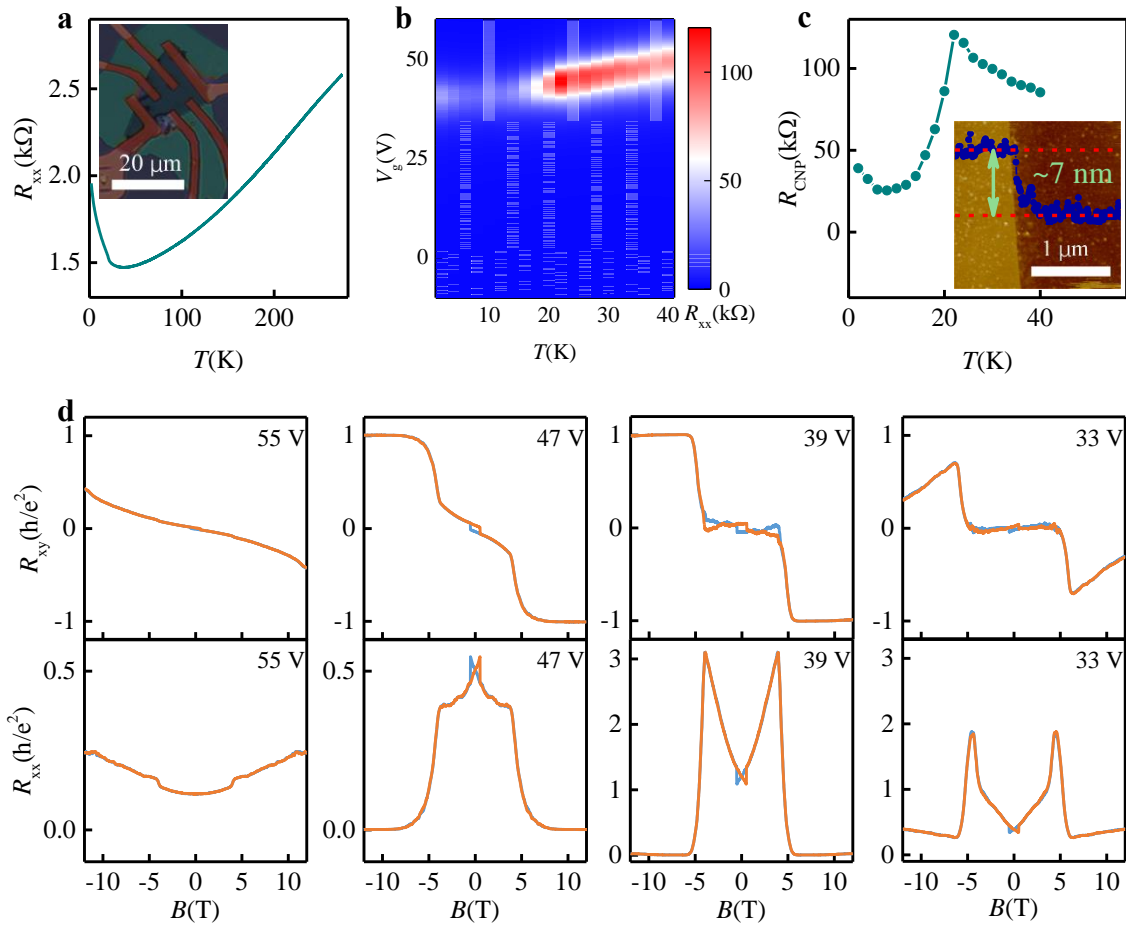


Figure 1

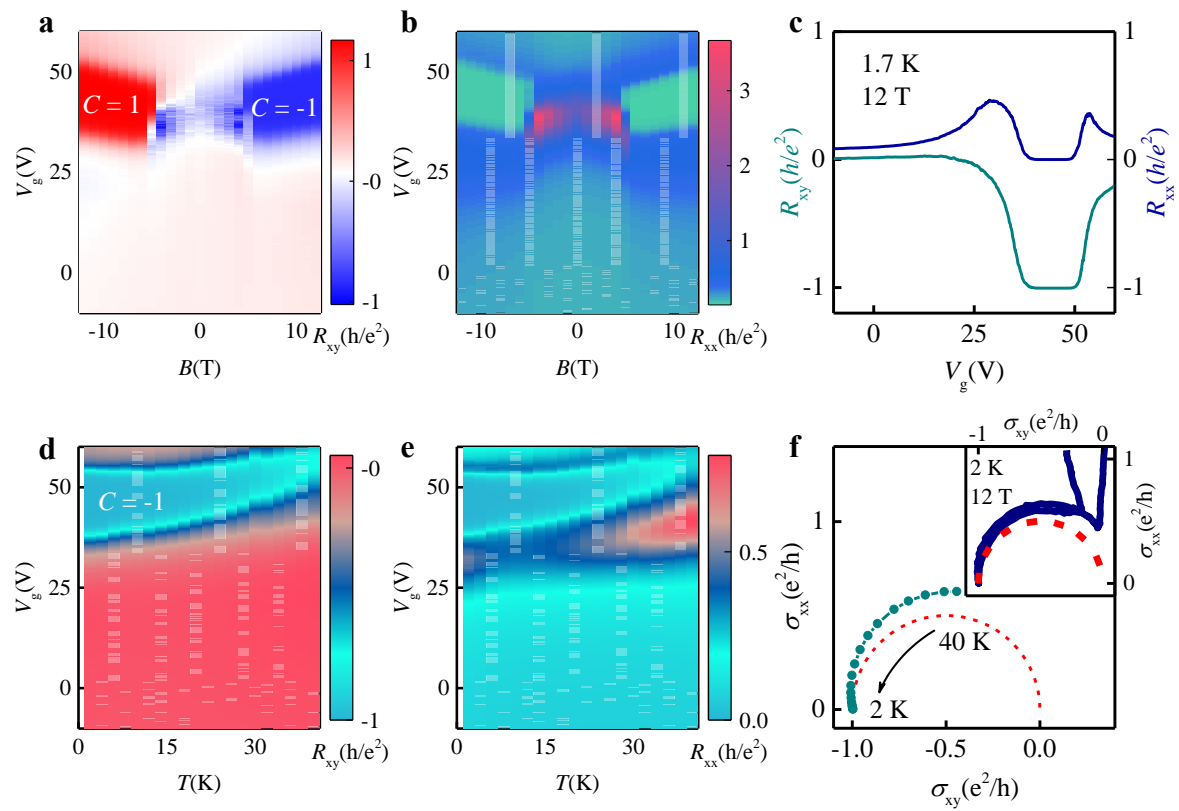


Figure 2

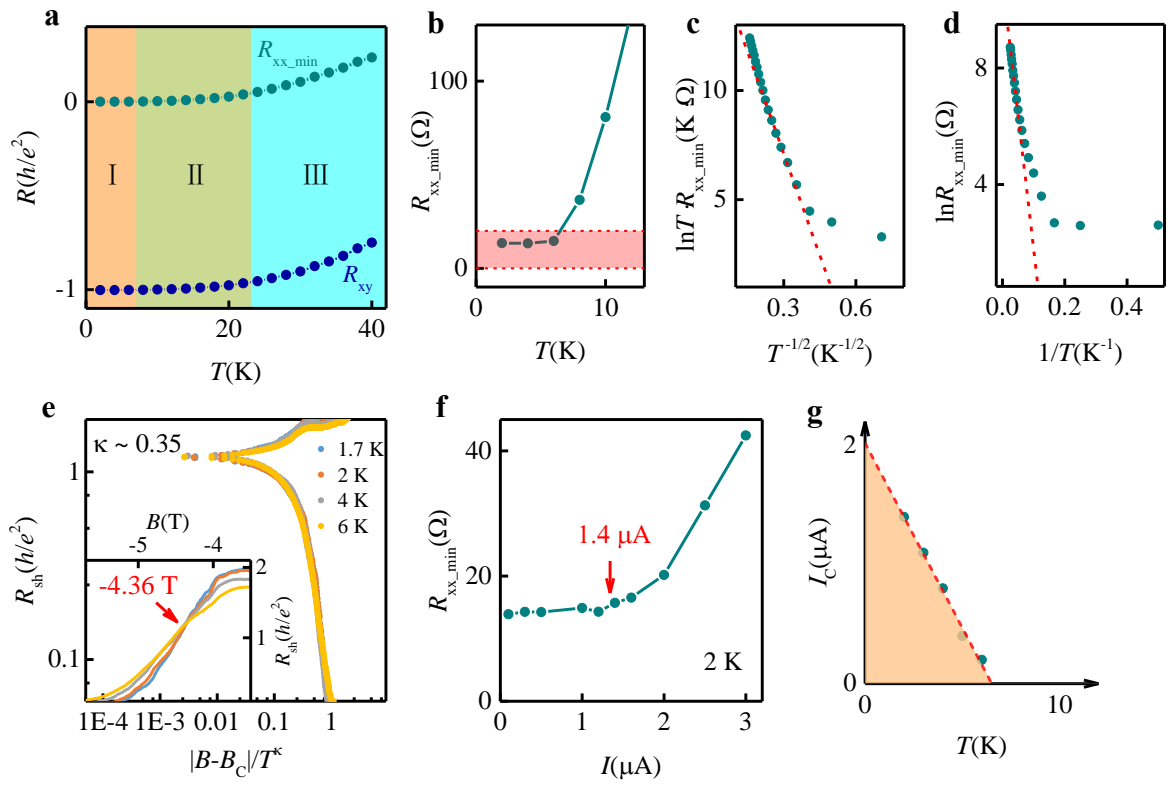


Figure 3

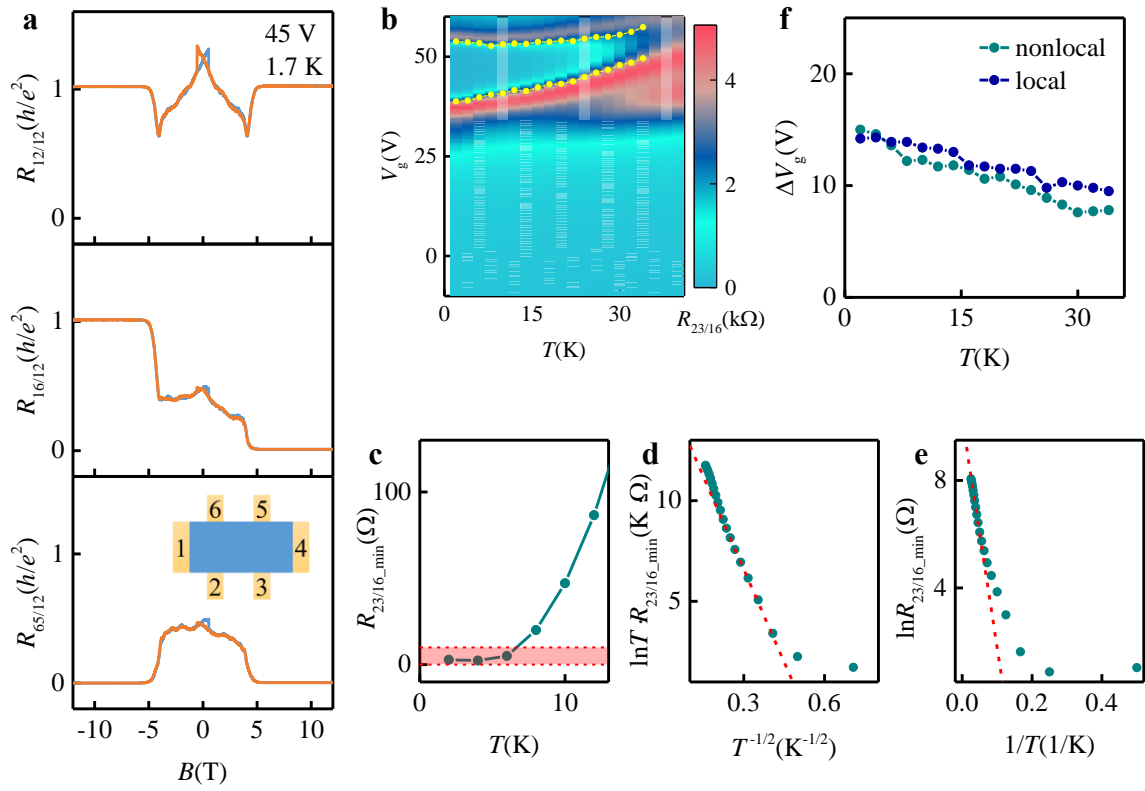


Figure 4